Planetary and Space Science 108 (2015) 108–116

Contents lists available at ScienceDirect

Planetary and Space Science

journal homepage: www.elsevier.com/locate/pss

A cone on Mercury: Analysis of a residual central peak encircled by an explosive volcanic vent

Rebecca J. Thomas [a,*], Alice Lucchetti [b,c], Gabriele Cremonese [c], David A. Rothery [a], Matteo Massironi [b,c,d], Cristina Re [c], Susan J. Conway [a], Mahesh Anand [a,e]

[a] Department of Physical Sciences, The Open University, Walton Hall, Milton Keynes MK7 6AA, UK
[b] CISAS, University of Padova, Via Venezia 15, 35131 Padova, Italy
[c] INAF—Astronomical Observatory of Padova, Vicolo dell'Osservatorio 5, 35131 Padova, Italy
[d] Department of Geosciences, University of Padova, via G. Gradenigo 6, 35131 Padova, Italy
[e] Department of Earth Sciences, The Natural History Museum, Cromwell Road, London, UK

ARTICLE INFO

Article history:
Received 30 May 2014
Received in revised form
27 October 2014
Accepted 19 January 2015
Available online 31 January 2015

Keywords:
Mercury
Explosive volcanism
Pyroclastic
Cratering
Hydrocode modelling

ABSTRACT

We analyse a seemingly-unique landform on Mercury: a conical structure, encircled by a trough, and surrounded by a 23,000 km^2 relatively bright and red anomaly of a type interpreted elsewhere on the planet as a pyroclastic deposit. At first glance, this could be interpreted as a volcanically-constructed cone, but if so, it would be the only example of such a landform on Mercury. We make and test the alternative hypothesis that the cone is the intrinsic central peak of an impact crater, the rim crest of which is visible beyond the cone-encircling trough, and that the trough is a vent formed through explosive volcanism that also produced the surrounding bright, red spectral anomaly. We test this hypothesis by comparing the morphology of the cone and the associated landform assemblage with morphologically-fresh impact craters of the same diameter as the putative host crater, and additionally, by modelling the original morphology of such a crater using a hydrocode model. We show that the present topography can be explained by formation of a vent completely encircling the crater's central peak and also make the observation that explosive volcanic vents frequently occur circumferential to the central peaks of impact craters on Mercury. This indicates that, although this cone initially appears unique, it is in fact an unusually well-developed example of a common process by which impact-related faults localize magma ascent near the centre of impact craters on Mercury, and represents an extreme end-member of the resulting landforms.

1. Introduction

Images acquired by the MErcury Surface, Space ENvironment, GEochemistry, and Ranging (MESSENGER) spacecraft since it went into orbit around Mercury in 2011 have revealed an unusual landform: a steep-sided cone that lies at the centre of a large diffuse-margined spectral anomaly that is bright and red-sloped compared to the Hermean average (Fig. 1). Spectral anomalies of this type elsewhere on the planet have been attributed to pyroclastic deposition (e.g. Kerber et al., 2009, 2011; Goudge et al., 2014), so this association suggests a landform genesis involving explosive volcanism. Volcanism builds steep-sided edifices on Earth and Mars by deposition of ballistically-ejected particles (e.g. Hasenaka and Carmichael, 1985; Brož and Hauber, 2012) or by flow of viscous lava. However, on Mercury, the ballistic range of particles ejected at a particular velocity is greater than on Mars and Earth, due to a lack of air-resistance and weaker gravity. For this reason, edifices formed in this way would be expected to have relatively low relief (McGetchin et al., 1974; Brož et al., 2014). Additionally, compositional data do not at present support the presence of evolved lavas capable of building steep-sided edifices through effusion (Denevi et al., 2013; Nittler et al., 2011; Weider et al., 2012). It would therefore be surprising to find that this cone is a volcanic construct. Indeed, studies of volcanic landforms on Mercury have thus far documented very little relief, with lavas forming smooth plains (Denevi et al., 2013) and deposition around vents attributed to explosive volcanism forming relief of only a few degrees (Head et al., 2008; Rothery et al., 2014; Thomas et al., 2014).

The specific morphology of the landform assemblage around the cone suggests an alternative hypothesis for its formation. The cone lies within an encircling trough, which is in turn encircled by a ridge. If the ridge is interpreted as the rim crest of a 43-km diameter impact crater, the cone occupies the location where a central uplift structure would be expected (Pike, 1988). In this scenario the bright, spectrally red-sloped deposit formed through

* Corresponding author. Tel.: +44 1908 858535.
E-mail address: Rebecca.thomas@open.ac.uk (R.J. Thomas).

http://dx.doi.org/10.1016/j.pss.2015.01.005

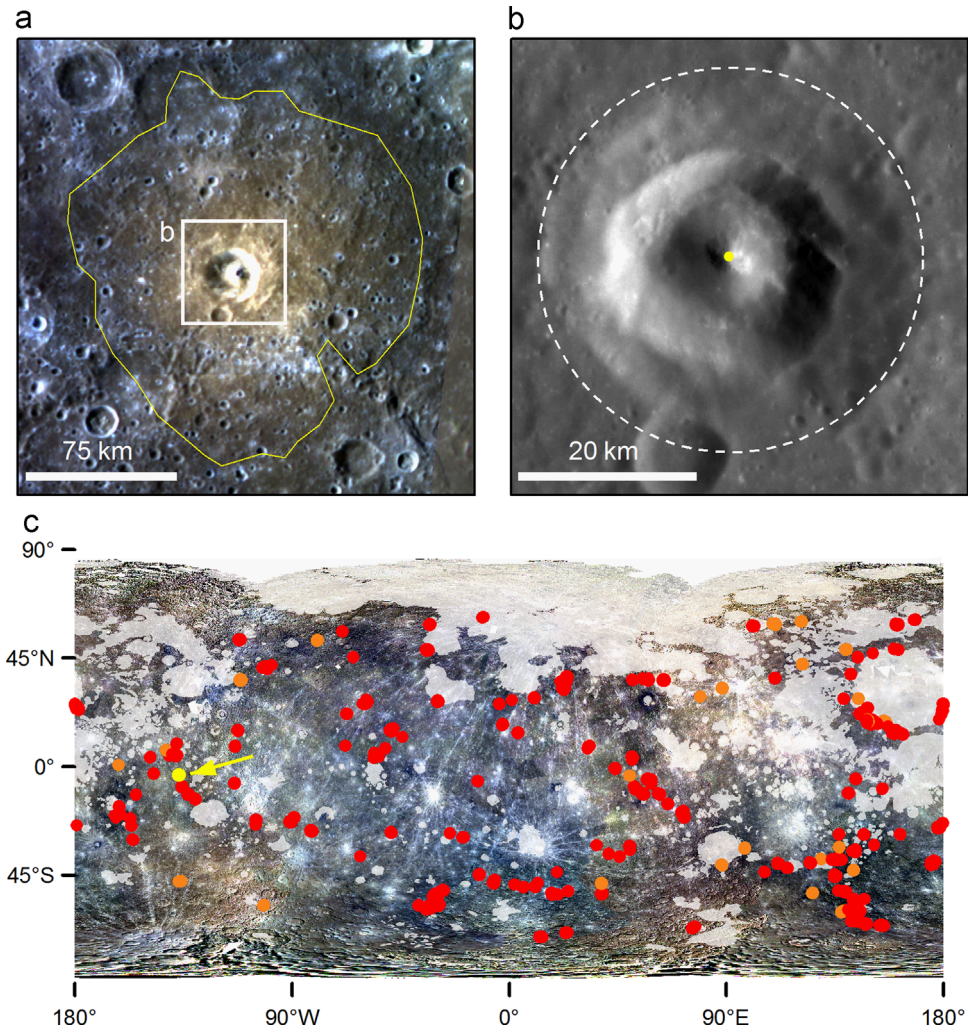

Fig. 1. A steep-sided cone associated with putative explosive volcanic products (−136.7°E, −3.5°N). (a) The cone lies at the centre of a widespread relatively bright and red-sloped spectral anomaly (yellow outline) characteristic of explosive volcanism. White rectangle: extent of (b). (Image: colour composite of images EW0262430050I, EW0262430054F and EW0262430070G). (b) Close-up showing that the cone lies within a pit, which is encircled by a ridge (dashed white line), interpreted as the rim-crest of an impact crater. Yellow dot: central point used for determining the median elevation profile in Fig. 3 (Image EN0212284006M). (c) Global location of the cone (yellow dot, yellow arrow) relative to endogenic pits with (red dots) and without (orange dots) a surrounding relatively bright and red-sloped spectral anomaly (identified by Thomas et al., 2014). White areas indicate smooth volcanic plains (from Denevi et al., 2013). (Base image: MESSENGER global colour mosaic v5). Images in (a) and (b) were obtained by MESSENGER's Wide-Angle (10.5° field-of-view) and Narrow-Angle Camera (1.5° field-of-view), respectively. (For interpretation of the references to color in this figure legend, the reader is referred to the web version of this article.)

explosive eruption from the trough, interpreted as a volcanic vent encircling the crater's central uplift. This would be consistent with the observation that pits associated with pyroclastic deposits on Mercury are co-located with regions of structural weakness in impact craters (Gillis-Davis et al., 2009), and would support the hypothesis that such structures play a controlling role in explosive volcanic eruptions on Mercury (Thomas et al., 2014).

In order to assess the viability of this hypothesis, we have investigated the probable original morphology of an impact crater of this size on Mercury by (i) measuring topographic cross-sections across relatively similar-diameter fresh craters, and (ii) performing a hydrocode simulation of the impact. These methods are complementary: while real craters indicate the range of crater morphologies that may arise on Mercury, their variation results from both primary factors (e.g. target heterogeneity, variations in volume of impact melt) and secondary factors (e.g. degradation, volcanic infilling). The simulation results are an aid to distinguishing these elements. We have compared both of these strands of evidence to the present morphology of the cone and associated landform assemblage to assess our hypothesis and to make quantitative inferences. We have also considered other crater-centered explosive volcanic vents on Mercury to assess whether this hypothesis is consistent with a general model for common mechanisms of explosive volcanic eruption on the planet.

2. Landform description and Proposed mode of formation

The steep-sided cone-like structure is surrounded by a 7 km-wide trench. This is in turn encircled by a topographic rise, which we interpret as the rim crest of a 43-km diameter impact crater (Fig. 1b). This landform assemblage lies at the centre of a 23,000 km^2 spectral anomaly with the relatively bright, red-sloped character that is attributed elsewhere on Mercury to pyroclastic deposits (Kerber et al., 2009; Goudge et al., 2014), which is the second most areally-extensive such anomaly on the planet (Thomas et al., 2014).

On Mercury, craters with a diameter greater than 12 km are expected to have a central uplift at the location where the cone occurs (Pike, 1988). We hypothesize that the first stage of formation of this landform assemblage was the creation of a 43-km diameter crater with a central uplift through an impact event (Fig. 2a). After an

unknown period, magma rose beneath the crater, either as a result of or independently of the impact crater formation (Fig. 2b). This magma may have stalled in the low-density fractured zone beneath the crater, in a manner similar to that hypothesized to result in floor-fractured craters on the Moon (Schultz, 1976). During a period of subsurface magma storage, crystallization of volatile-poor minerals may have enhanced the volatile content of the remaining melt. When either volatile overpressure or magma driving pressure favoured further dyke propagation, this occurred subvertically due to the presence of zones of weakness in the overlying crust (Parfitt et al., 1993), particularly high-angle faults bounding the central uplift (Senft and Stewart, 2009; Scholz et al., 2002; Kenkmann et al., 2014). The resultant eruption of volatile-rich magma formed the trench, a vent that entirely encircles the central uplift, and emplaced pyroclastic deposits to form the surrounding spectral anomaly.

To test this hypothesis, we examine the morphology, dimensions and topography of the cone, pit, host crater and deposit, and we also compare the present-day topography with two estimates of the original host crater topography: the topography of fresh craters of a similar size that are not associated with pyroclastic deposits and hydrocode impact modelling. For brevity, we will refer to this crater as AP1 in this paper ('Annular Pit 1')

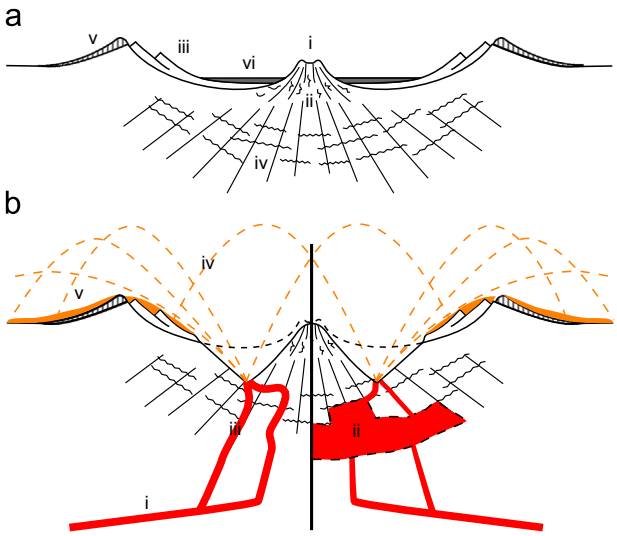

Fig. 2. Proposed model of formation of a crater-centered cone surrounded by pyroclastic deposits by vent formation around the central uplift of the impact crater. (a) Schematic of a complex impact crater with (i) a central uplift with (ii) internal steeply-dipping faults (Senft and Stewart, 2009; Scholz et al., 2002), (iii) slump structures forming terraces, (iv) an underlying fracture zone (Schultz, 1976; Kenkmann et al., 2014), (v) ejecta and (vi) impact melt deposits forming a flat floor. (b) Proposed morphology of the crater during explosive volcanic activity, with (left) or without (right) shallow magma storage. (i) Volatile-bearing magma rises from depth along a sill or dyke, possibly forming (ii) a shallow magma chamber or sill beneath the low density fractured zone (right; dashed outline indicates the margins may be gradational). (iii) Dyke propagation to the surface occurs along planes of crustal weakness, possibly aided by an increase in overpressure due to volatile exsolution. (iv) Volatiles within the magma expand at the surface and eject juvenile and vent-wall material. This falls along ballistic pathways to form (v) deposits with a relatively bright and red-sloped spectral character (dashed line indicates the original crater profile).

3. Methods

3.1. Planform morphology

To investigate the planform morphology of the cone and associated deposits, we examined all images of the study location taken by the MDIS camera onboard MESSENGER with product creation times up to September 17, 2013. MDIS consists of a 1.5° field-of-view monochrome Narrow Angle Camera (NAC), and a 10.5° field-of-view multispectral Wide Angle Camera (WAC). We performed radiometric and photometric corrections on all images using the ISIS3 (Integrated System for Imagers and Spectrometers) software produced by the U.S. Geological Survey. Because the WAC takes repeated images of the same location through filters at different wavelengths, we were able to combine reflectance at 966 nm, 749 nm and 433 nm in the red, green and blue bands to produce colour images. This combination allows discrimination of relatively bright and spectrally red-sloped pyroclastic deposits (Kerber et al., 2009; Goudge et al., 2014) despite the generally subtle contrast in albedo and colour between regions of Mercury's surface (Denevi et al., 2009).

We used Graphics and Shapes tools (Jenness, 2011) within ArcGIS software to make geodetic planform measurements of the dimensions of the cone, associated landforms and deposit.

3.2. Present-day topography

Due to MESSENGER's highly elliptical orbit around the planet, the Mercury Laser Altimeter (MLA) has not been able to obtain

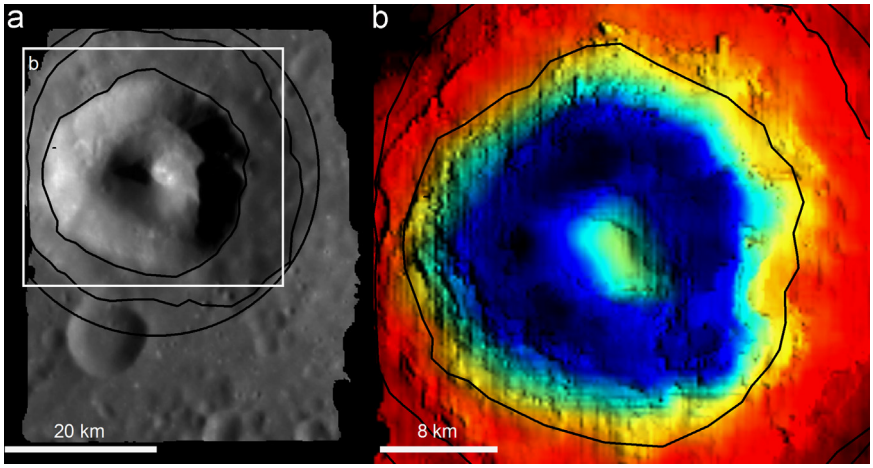

Fig. 3. Extent of the stereo-derived DTM of the cone and surrounding pit and crater (based on images EN0257648861M and EN0227259475M). (a) An orthorectified image showing the extent of the DTM. Black lines indicate the position of the pit and crater rims. White rectangle: extent of (b). (b) Colorized shaded relief produced from the DTM (blue, green, red indicate increasing elevation) showing irregularities in the depth of the pit floor, probably mass wasted material. (For interpretation of the references to color in this figure legend, the reader is referred to the web version of this article.)

elevation data at the location of interest to this study. We therefore determined the present-day topography by creating a digital terrain model (DTM) using NAC stereo images EN0257648861M and EN0227259475M. Correlation of the images was performed using the area-based image matching software, Dense Matcher (Re et al., 2012). The Ames Stereo Pipeline (Moratto et al., 2010) was then used to triangulate from this data and produce a 215 m/pixel DTM (Fig. 3). The DTM has approximately 1 pixel (215 m) horizontal accuracy and 100 m vertical accuracy.

3.3. Original crater topography

To investigate the geological processes that formed the cone and estimate the volume of material involved, it is necessary to determine the probable morphology of the planet's surface at this location prior to its creation. As the cone lies at the centre of an impact crater, this can be approximated by estimating the original morphology of the host crater. We investigated this using two complementary methods, as follows.

3.3.1. Topography of undegraded craters of a comparable size

We identified three 42–47 km diameter impact craters where a MLA track crosses the central peak structure and approximately bisects the crater (Fig. 4). These were used as a control on crater morphology and to assess the plausibility of the results of our simulations. We specifically chose impact craters with thick proximal ejecta blankets and little sign of terrace modification, indicating that they are relatively undegraded (Mansurian age, 3.5–1 Ga) (Spudis and Guest, 1988), and therefore approximate the morphology of the impact crater being studied not long after its formation. We note with caution that the pyroclastic deposits obscure the original topography of AP1, so we cannot visually assess how degraded it was prior to the pyroclastic activity.

3.3.2. Impact crater numerical model

We simulated the formation of the impact crater using the iSALE (Impact Simplified and Arbitrary Lagrangian Eulerian) hydrocode, one of several multirheology, multimaterial extensions of the SALE hydrocode (Amsden et al., 1980). This has been specifically developed to model impact crater formation in its entirety (Melosh et al., 1992; Ivanov and Kostuchenko, 1997; Collins et al., 2004; Wünnemann et al., 2006) and performs well in reproducing the results of laboratory experiments at high strain-rates (Pierazzo et al., 2008).

The structure and composition of the projectile was simplified to spherical and homogeneous basalt impacting at an angle of 90°. Departure of the impact angle from the more statistically likely value of 45° is necessary due to the axisymmetric nature of the iSALE hydrocode. The only way to take the effect of different impact angles into account is to assume that the projectile has an average impact speed, but impacts at 45° impact angle. Therefore, the impact speed used in the simulation is (v_average) × sin(45°), and we assume an impact velocity of 30 km/s, derived from an average impact velocity of 42 km/s (Marchi et al., 2005). We estimated a porosity of 10%, derived from the average of meteorite types proposed by Britt et al. (2002). We estimated an impactor size of 2.4 km diameter by comparing profiles obtained in a series of runs at low resolution to the topographic profile of the present topography and cross-sections of the similar-sized control craters. We took an Eulerian approach, defining the number of computational cells per projectile radius (CPPR) as the resolution of our impact model. We used the Eulerian setup because of the inevitable extreme cell deformation that occurs with the alternative Lagrangian approach (Pierazzo and Collins, 2004). The crater was modelled on a computational mesh of 400 × 600 cells, with a cell size of 150 m and a projectile size of 8 CPPR. We used a spatially constant gravitational acceleration of 3.7 m/s^2.

We approximated the Hermean surface as a homogeneous layered half-space made up of a jointed 5 km basalt layer overlying an intact basalt layer. This depth was chosen on the basis of the thickness estimation of the fractured layer derived by Schultz (1993) and on the crater size frequency distributions predicted by the MPF (Model Production Function) for analogue smooth plains (Marchi et al., 2011; Giacomini et al., 2014). The material properties of these layers are summarized in Table 1.

The output morphology of the simulation is dependent on the equations of state and constitutive (material strength) models incorporated into the hydrocode. Therefore, the thermodynamic response for both the projectile and target in our simulations was approximated with an equation of state for basalt derived using the ANEOS model (Thompson and Lauson, 1974). The rock strength model employed in iSALE, which accounts for changes in material shear strength (Collins et al., 2004), also includes a transient weakening mechanism called acoustic fluidization that allows the development of the central peaks and terraced walls through gravitational collapse (Wünnemann and Ivanov, 2003). iSALE adopts a simple mathematical approximation of Acoustic Fluidization (AF), known as the Block Model, that is controlled by two parameters: the kinematic viscosity of the fluidized region and the decay time of the block vibrations. We performed simulations over a broad parameter space to determine the parameters producing the best fit to the dimensions of the crater being studied, and then selected between those produced at different kinematic viscosities on the basis that the final result should be consistent with the morphology of the crater being studied and the control craters.

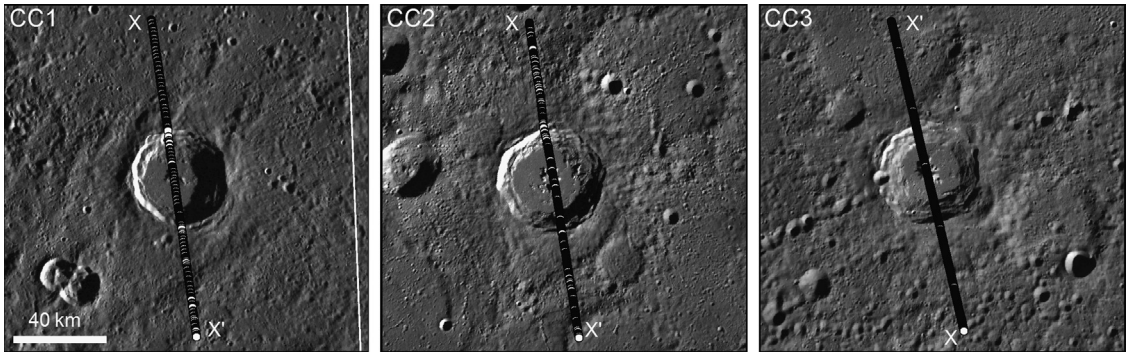

Fig. 4. ~43 km Diameter morphologically fresh impact craters used as a control on the original crater shape and on the simulation. Outlined dots indicate MLA data points from X to X′ used in Fig. 6. CC1: 177.1°E, 50.9°N, MLA track MLASCIRDR1109231307 (orbit 380); CC2: −107.5°E, 49.2°N, MLA track MLASCIRDR1208272313 (orbit 1198); CC3: −122.1°E, 63.8°N, MLA track MLASCIRDR1203061631 (orbit 715). Only channel 1, high threshold, MLA pulse returns were used to avoid incorporating noise. All the panels have the same horizontal scale as that indicated for CC1 (Base image: MDIS global monochrome mosaic v9).

4. Results

4.1. Present-day morphology and deposit extent

The stereo-derived DTM reveals the topography of the cone, pit and all but the far western rim of the crater (Fig. 3). The cone has a basal diameter of ~12.5 km. It stands up to 2.2 km above the floor of the pit surrounding it and its summit is 1.8 km below the rim crest of the host crater (Fig. 5). It lacks a summit crater and has steeply-dipping flanks, averaging 26°. The pit margins are similarly steep, averaging 30°. The pit floor is shallower in some places than others, consistent with landsliding from the wall scarps (Fig. 3b). This suggests that the original slope of the pit walls may have been greater prior to mass wasting.

The crater's average diameter is 43.2 km. The area between the rim-crest (defined as the summit of the topographic rise around the pit) and the outer pit margin measures on average 8.5 km wide on the orthorectified image, has a smooth texture, and forms a 'step'. This may be a terrace formed by wall-slumping, draped by volcanic deposits.

The surrounding bright, red-sloped spectral anomaly has a maximum extent of 92 km from the centreline of the pit.

4.2. Topography of the control craters

Craters CC1, CC2 and CC3 have diameters of 41.8 km, 46.7 km and 43.2 km, respectively. For comparison with the present-day topography of AP1, distances in the cross-sections were normalised to give a crater diameter of 43.2 km. Because a smaller impact crater would be expected to have a smaller ratio of rim-crest to floor depth, this necessitated a relatively minor adjustment to elevation values across CC1 and CC2. This was made by first calculating the expected rim crest to floor depth (d) of the crater on the basis of the relationship of this value to diameter (D) observed by Pike (1988) for complex craters on Mercury:

$$d = 0.353D^{0.496} \quad (1)$$

We calculated the ratio between the depth indicated by this method for the control crater and for a 43.2-km diameter crater and multiplied the MLA elevation values by this value.

To compare the morphology of the craters, we have plotted them so that distance along the cross-section is equal at the rim crest and elevation is equal at the base of the outer slope of the raised rim (known as the rim flank). The latter feature was chosen as the best point of reference because the topography beyond the craters (Fig. 6a) is very uneven due to the presence of other impact craters, so it is impractical to identify a 'regional datum' at any greater distance. Because the elevation of the rim crest itself is particularly vulnerable to degradation processes, this too was judged an uncertain point of reference. The control craters have similar profiles, excepting that the floors of CC1 and CC2 are shallower (2.3 km and 2.1 km) and the peak height above the floor is lower (0.4 km and 0.7 km) than those of CC3 (with a depth of 2.7 km and a peak height of 1.2 km) (Fig. 6a). This suggests that the interiors of CC1 and CC2 have experienced more infilling than CC3, either by retention of a higher volume of impact melt during the modification stage of their formation, or by post-formation volcanic flooding.

Table 1
Strength model parameters for the impacted surface used to simulate the original morphology of the crater being studied.

Variable	Description	Jointed basalt	Intact basalt
Y_0	Cohesion for intact material (MPa)	10	10
Y_d	Cohesion for damaged material (MPa)	0	1
Y_m	von Mises plastic limit (GPa)	3.5	3.5
μ_i	Coefficient of internal fiction	1.2	1.2
μ_d	Coefficient of friction (damaged material)	0.6	0.6
T_m	Melt temperature (K)	1500	1500

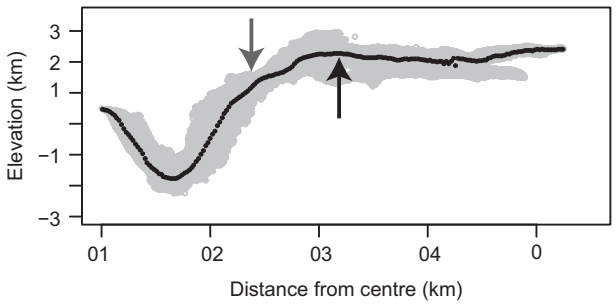

Fig. 5. Present-day topography of the crater. (a) Average present-day topography from the centre of the cone. Light grey circles mark the elevation of each pixel of the DTM against its distance from the cone centre. Black dots mark the median elevation within 215 m radial bins. Grey arrow: average location of the pit margin, black arrow: average location of the rim crest.

4.3. Numerical simulation

A projectile with a diameter of 2.4 km, penetrating the target at 30 km/s (in accordance with Marchi et al., 2005), generates a crater diameter in agreement with the DTM profile considering that the final output of iSALE has a 4% radius uncertainty (a value found from code validation against laboratory experiments (Pierazzo et al., 2008)) (Fig. 6a). The simulation shows a best fit with the crater diameter and the interior morphology of the control craters with a decay time of 48 s and a kinematic viscosity of 120,000 m/s^2. As with the control craters, both horizontal and vertical values along the simulated cross-section were adjusted for comparison to a 43.2-km diameter crater.

Results from the simulation are in accordance with depth-diameter ratios observed in impact craters in large morphometric datasets for Mercury. Pike (1988) finds a best-fit to the depth-diameter values of 58 craters between 30 and 175 km diameter with the relationship given in Eq. (1). Using this relationship, a 43.2 km wide crater would be expected to be 2.3 km deep; the simulated crater has a depth of 2.3 km (2.1 km after adjustment of its depth to take into account its greater diameter). Baker and Head's more recent study (2013) using MESSENGER data found a mean depth-diameter ratio of 0.034 ± 0.010 for complex craters greater than 50 km in diameter. If we apply this to the crater we are studying, it predicts a depth of 1–1.9 km: shallower than the simulated crater, but this may be a result of extrapolating their observed relationship to a sub-50 km diameter crater. Using a similar method of extrapolation for peak height data in the same work, the expected height of the central peak would be in the range of 0.3–0.9 km. The height of our simulated central peak above the crater floor is 600 m, or 570 m after adjustment for the greater crater diameter, and so is in agreement with this estimation. This indicates that though the simulated central peak is lower than those of the control craters, it lies within the range of observed values on Mercury. The simulated central peak width (8.7 km, or 7.8 km after adjustment for crater diameter) is somewhat narrower than the relationship

$$D_{cp} = 0.44D^{0.82}, \quad (2)$$

observed by Pike between crater diameter D and central peak width D_{cp} in 138 craters: this predicts a width of 9.7 km.

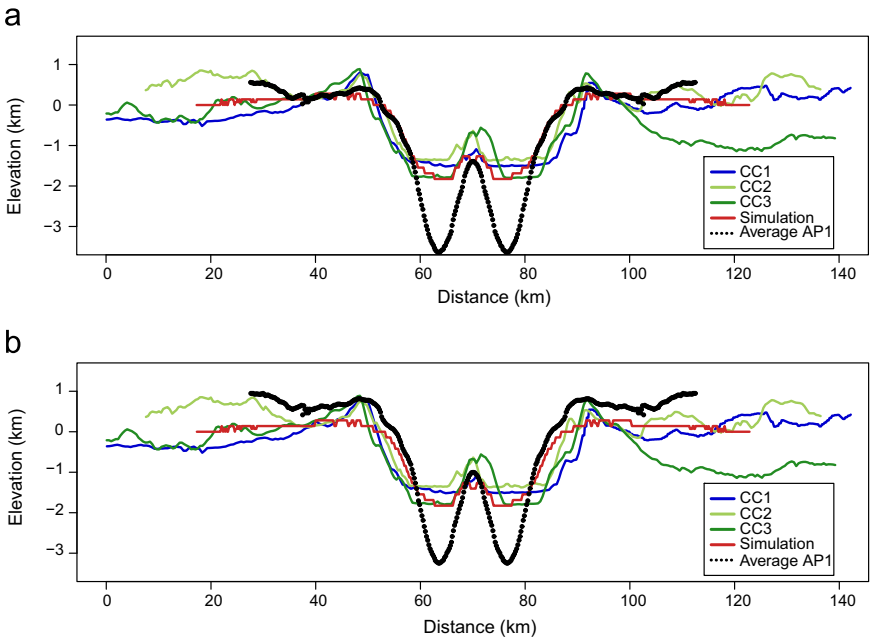

Fig. 6. (Color online) Comparison between the average DTM elevations across the present-day landform, MLA cross-sections through the control craters, and the results of the hydrocode simulation, showing general agreement between complex crater morphology and the morphology of the cone in AP1. (a) Values on the distance axis are equal at the leftmost rim crest, and elevations are equal at the base of the leftmost rim flank. (b) Horizontal location and elevations are matched as in (a), except that the DTM profile is placed so that the rim-crest elevation equals the average elevation of the leftmost rim crests of the control craters.

When vertically matched with the control craters at the base of the rim flank, the elevation of the floor of the simulated crater almost exactly matches that of CC3, which we have previously identified (Section 3.1) as the least likely to have undergone significant infilling. However, the morphology of the simulation differs from that of the control craters in several aspects: the height of the rim crest relative to the base of the rim flank is much lower (140 m) versus an average of 780 m in the control craters, the walls are narrower, especially at high elevations, as a result of a broader (~4 km versus 1.6 km or less) shallowly-sloping region inwards of the rim crest, and there are no wall terraces. As the simulation indicates the crater morphology at the end of the modification stage of crater-formation, 1500 s after impact, these differences may result from an incomplete simulation of post-formational wall and rim modification resulting, for example, from long-timescale crustal response (Kenkmann et al., 2014). These differences reinforce the value of looking at both strands of evidence to indicate the range of possible morphologies for AP1 during the period of volcanic activity.

4.4. Comparison of estimated original and present morphologies

We compare the present topography with the control craters and the simulated original topography using two possible vertical tie-points. The first plots all cross-sections so that the elevation at the base of the rim flank is equal (Fig. 6a). This requires the assumption that there is not an appreciable thickness of pyroclastic material in this area, as this would increase the elevation of the original ground surface. The second comparison plots the topographic profile derived from the DTM such that its rim crest is at the average elevation of the rim crests of the control craters (Fig. 6b). This would be a valid match if the original crater AP1 has undergone a similar amount of degradation as the control craters and if pyroclastic deposition has not increased the ground elevation at the rim crest. We judge that the first comparison leads to a better match between the interior and exterior morphology of AP1 and the morphology of the simulated and control craters, so we prefer to use this in the proceeding analysis.

The height of the cone (820 m above the expected floor height indicated by CC3 and the simulation, and 1.4 km below the rim crest) is consistent with that expected on the basis of the simulation and the control craters (Fig. 6a) and with the relationship to crater diameter observed by Baker and Head (2013) in >50 km diameter craters on Mercury (which predicts a height of 0.3–0.9 km above the crater floor). The width of the cone at the elevation of the floors of the simulated crater and CC3 is 4.3 km, which is narrower than expected for the central peak of a crater of this size (9.7 km) (Pike, 1988). The wall-to-wall distance below the 'step' in the crater topography inwards of the rim crest is similar to that of the simulation, but narrower than in the control craters. There are three possible explanations of this. One is that this morphology is original to the crater, and results from the post-formational modification of AP1 being arrested at an earlier point than is normal. Such a phenomenon is not observed at other craters on Mercury, so we judge it improbable. The second is that the 'step' was created by wall slumping. This is very credible, as wall terraces resulting from slumping are seen in all three control craters and are characteristic of impact craters of this size on Mercury (Pike, 1988). The third is that the walls have been covered by a thick layer of pyroclastic material. There is some evidence for pyroclastic deposition in the region between the rim crest and the pit margin: it has the same smooth texture here and outside the rim, with no boundary between the two surfaces (Fig. 1b). Pyroclastic deposits may thus contribute to the broad, high-elevation region inwards of the rim crest and the relative narrowness of the crater walls. However, it is not possible to distinguish relief resulting from pyroclastic deposition from that resulting from crater modification and degradation processes.

The pit represents a large loss of material: if the simulation and present-day DTM topography are vertically matched as in Fig. 6a, the average pit floor is 1.4 km below the expected crater floor depth, and the volume difference (calculated using ArcGIS) is ~350 km^3. If a similar comparison is made to a DEM constructed with elevation plotted radially against distance from the crater centre to the northern rim of CC3, the volume of material missing within the trench and cone area of AP1 is ~300 km^3. These are approximate values for the volume of material lost because

shadows in the images used to construct the DTM do not allow us to calculate the volume loss in the eastern part of the pit, and because the vertical match is uncertain.

If the volume loss from the pit equals the volume of a pyroclastic deposit over the area indicated by the bright, red-sloped spectral signature, that deposit would average ~20 m thick using the volume change indicated by the hydrocode, or ~17 m thick using the volume difference from CC3, when scaled to take into account the different densities of basalt rock and pyroclastic fall (2760 kg /m^3 vs. 2000 kg/m^3 (Wilson et al., 2014)). Elsewhere on Mercury, putative pyroclastic deposits ranging from 29 to 567 m thick have been identified in close (~6 km) proximity to vent margins (Thomas et al., 2014). Where such relief is observed, the surrounding relatively bright and red-sloped spectral anomaly extends to an average of three times as far from the vent margin, indicating the presence of an outer zone of thinner (and, at current resolutions, topographically undetectable) deposits. Because of the uncertainties of the vertical match between the original and present-day topography, we cannot determine whether deposits at AP1 are thicker near the vent than at greater distances, though if, as discussed above, the wide high-elevation area inwards of the rim crest and the narrowness of the crater walls are in some part the result of pyroclastic deposition, this deposition would have occurred within 9 km of the pit margin.

5. Discussion

5.1. Mode of formation of the landform assemblage

There is no evidence that the cone was constructed by volcanism: it lacks a summit caldera or vents, has no flow features on its flanks and has a similar slope to that of the outer scarps of the pit surrounding it. Conversely, its position, elevation, slope and morphology is consistent with a residual central peak of an impact crater, surrounded by an annular pit.

The occurrence of a pit associated with pyroclastic deposits at the centre of an impact crater is not unique to this location. In a global survey we identified 150 sites were endogenic pits are surrounded by a bright, red-sloped spectral anomaly interpreted as pyroclastic deposits (Thomas et al., 2014). A total of 118 of these occur within impact craters, and 52 (excluding AP1) are at the crater centre (Supplementary Table 1). In some cases the pit is in place of an expected central peak or peak ring, but in 31 cases it is concentric to the peak or central region (Fig. 7). In some cases small pits occur around the crater centre (Fig. 7c), in others, conjoined pits form arcs around the centre (Fig. 7b), and in rare cases (e.g. Fig. 7a), a pit or conjoined pits entirely encircle the crater centre, though not forming so distinctive a 'cone' as seen at AP1. These configurations form a continuum and may represent a time sequence in which, with continued or repeated eruptions, pits around a crater's central peak enlarge and conjoin until they form a continuous trench encircling the peak. This indicates that the cone and trench at AP1 are an extreme end-member of a characteristic landform association on Mercury.

Terrestrial seismic surveys and numerical models give some indication of why vent-formation is localised in the vicinity of central peaks: they indicate that impact crater central uplifts are bounded by deeply-penetrating high-angle faults (Scholz et al., 2002; Senft and Stewart, 2009; Kenkmann et al., 2014). Mercury has been in a global state of compression for much of its history (Strom et al., 1975), inhibiting the ascent of magma to the surface, so it is to be expected that any magma ascent that did occur would be localised in pre-existing zones of weakness such as these. It is interesting to note that, though as has previously been stated (Gillis-Davis et al., 2009), endogenic pit formation appears to be structurally-controlled by host crater structures, our findings suggest that pits most commonly occur at the crater centre or along a peak ring, and less commonly at other fault-bounded structures such as the terraces or rim area. In contrast, on the Moon, volcanic vents within impact craters commonly occur at the margins of the crater floor (e.g. Head and Wilson, 1979; Head et al., 2000; Gaddis et al., 2013). This may indicate that either the mechanisms of magma ascent or the relative strengths of different parts of impact crater structures differ on the two bodies.

5.2. Mode of pit formation

A structural control on pit formation has been taken as evidence that Mercury's endogenic pits form by collapse along planes of weakness during magma withdrawal from a shallow magma chamber (Gillis-Davis et al., 2009). It is possible that subsidence has occurred in our example: the summit of the cone is 1.4 km below the rim crest, versus an average depth of 1.6 km for the control craters, despite probable degradation of the rim crest area of AP1 by 400 m. However, given the wide range of observed peak heights within complex craters (Baker and Head, 2013), and the absence of a crater floor relative to which the peak can be measured, this low peak elevation cannot be conclusively attributed to post-formation modification.

The pit was clearly the locus of intense explosive volcanism, so it is probable that a significant amount of wall-rock erosion contributed to pit-formation (and possibly reduction in peak height and width). The maximum dispersal of pyroclasts ejected on ballistic trajectories in the airless conditions of Mercury, as discussed by Kerber et al. (2009), is $X = v^2 \sin 2\theta / g$. Taking X as 92 km, the maximum horizontal radius of the deposit from the pit centreline, g (gravity) as 3.7 m/s^2 and θ as the angle at which dispersal is greatest (45°), the minimum velocity at the vent is 580 m/s. On Earth, such velocities are typical of high-energy Plinian eruptions, in which significant vent-widening occurs (Wilson et al., 1980). However, we do not know the volume of material ejected at this velocity, so it is not possible to quantify the kinetic energy available for wall erosion.

We await with interest higher-resolution compositional data, to be acquired as MESSENGER's orbit descends to lower altitudes and by the forthcoming BepiColombo mission (Fraser et al., 2010; Rothery et al., 2010). This may allow us to constrain the proportions of juvenile and non-juvenile material in the pyroclastic deposits and thus determine the relative importance of magma chamber drainage versus wall-rock excavation for pit formation.

5.3. Evidence for magma storage prior to eruption

Previous work (Thomas et al., 2014) has suggested that the horizontal scale of the largest pyroclastic deposits on Mercury (of which the 92 km radius AP1 deposit is the second-largest example) is consistent with their emplacement by either strombolian eruption or by high flux steady eruption where the majority of the magma is disrupted into large particles, 10 mm to 1 m diameter (Wilson and Head, 1981). Both strombolian eruption and eruption of predominantly large clasts indicate a slow magma rise speed, as a large particle size and intermittent, strombolian eruption are both caused by bubble coalescence prior to eruption. This suggests that the magma may have been stored beneath the crater prior to eruption.

The extreme dispersal of the deposits indicates a high volatile content in the magma. If we follow the method of Wilson et al. (2014) to calculate the released gas fraction on the basis of the gas speed at the vent (as discussed by Thomas et al., 2014) we find that that ejection of pyroclasts to 92 km on Mercury requires 5.4 wt% CO_2 or 4.2 wt% H_2O if each of these were the sole volatile. These

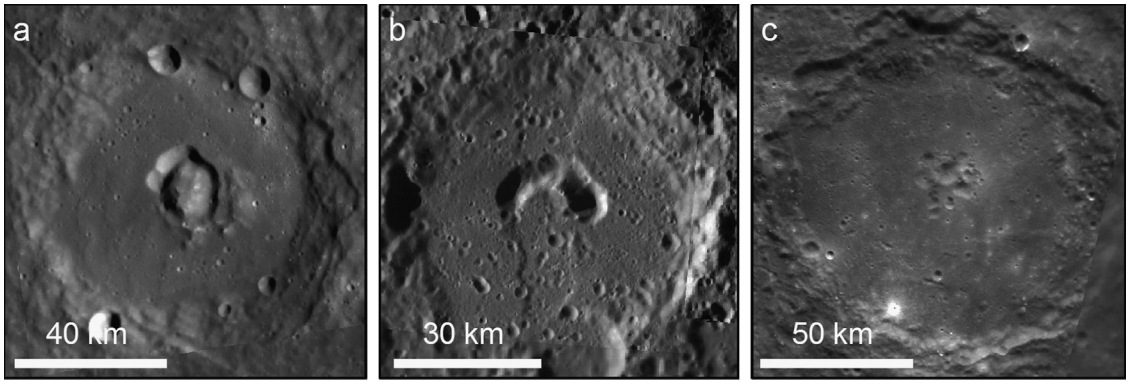

Fig. 7. Endogenic pits with surrounding pyroclastic deposits circumferential to the impact crater centre. (a) A pit entirely encircles the central uplift (72.4°E, −21.1°N). (b) Pits circumferential to the centre of an impact crater where the central peak is not visible, probably due to volcanic infill prior to pit formation (140.5°E, −11.1°N). (c) Multiple small pits occurring circumferential to the crater centre (6.5°E, −48.4°N).

are very high values: in non-subduction settings on Earth, melt inclusions indicate 0–0.25 ppm CO_2 and 0.2–0.8 wt% H_2O in basaltic melts (Metrich and Wallace, 2008). Chemical equilibrium models suggest a combination of more reduced species such as N_2, CO, S_2, CS_2, S_2Cl, Cl, Cl_2, and COS would be present in Mercury's magmas (Zolotov, 2011). Due to their high molecular weights, a concentration greater than, or equal to, 7.6 wt% would be necessary to form the deposit if any of them were the sole volatile. As there is no reason to believe Mercury to be more volatile-rich than Earth, it is probable that such high volatile concentrations were reached by some process causing volatile enrichment in the erupted magma (Thomas et al., 2014). Slow magma rise and/or storage at shallow depths could achieve this, as this would allow accumulation of exsolved gas prior to eruption. We note, however, that it is possible that some of the volatile enrichment may result from incorporation of volatile-bearing wall-rock, which could occur in steadily-rising magma that did not undergo a period of storage.

6. Conclusions

Our results confirm the hypothesis that a steep-sided cone surrounded by putative pyroclastic deposits on Mercury was formed by explosive volcanic eruption from a vent encircling a residual central peak of an impact crater. We find that the landform at this location likely represents the extreme end-member of a large class of volcanic vents circumferential to impact-crater central peak structures, indicating that crater-related faults control explosive volcanism at such locations. The scale of the pyroclastic deposit indicates that the magma had a high volatile content relative to basaltic eruptions on Earth, supporting the idea that it was stored for some time in the low-density fractured zone beneath the impact crater prior to eruption.

It is interesting to note that a similar process, where magma ascends to the fractured zone beneath an impact crater, stalls and, in some cases, erupts explosively due to pressure build-up resulting from volatile accumulation, is also hypothesised for the Moon (Head and Wilson, 1979). On the Moon, however, the crater floor becomes fractured by inflation of a sub-crater laccolith (Schultz, 1976; Jozwiak et al., 2012) and dyke propagation to the surface is favoured by this fracturing, usually occurring from the crater floor adjacent to the walls. Additionally, surrounding putative pyroclastic deposits are, on average, less areally-extensive than those observed on Mercury (Thomas et al., 2014). The observation that endogenic pits commonly occur at the centre, rather than at the margins, of impact craters on Mercury, and a lack of floor-fracturing, suggests a difference in the processes by which crater-hosted explosive volcanism occurs on the two small, airless bodies. Future comparative study may prove fruitful for our understanding of the processes at work on both the Moon and Mercury.

Acknowledgements

Rebecca Thomas acknowledges support via a PhD grant from the Science and Technology Facilities Council (UK) (Grant no. ST/K502212/1) and David Rothery acknowledges support from the UK Space Agency (Grant nos. PP/E002412/1 and ST/M002101/1) in preparation for the BepiColombo mission. This research was also supported by the Italian Space Agency (ASI) within the SIMBIOSYS Project (ASI-INAF agreement no. I/022/10/0).

We gratefully acknowledge the developers of iSALE, including Gareth Collins, Kai Wünnemann, Dirk Elbeshausen, Boris Ivanov, and Jay H. Melosh (see www.iSALE-code.de).

The image and MLA data used in this paper are available at the PDS Geosciences Node of Washington University, St. Louis, U.S.A. All other data are available from the authors on request.

Appendix A. Supporting information

Supplementary data associated with this article can be found in the online version at http://dx.doi.org/10.1016/j.pss.2015.01.005.

References

Amsden, A.A., Ruppel, H.M., Hirt, C.W., 1980. SALE: A Simplified ALE Computer Program for Fluid Flow at All Speeds. Los Alamos National Laboratory LA p. 8095 (Los Alamos, NM).

Baker, D.M.H., Head, J.W., 2013. New morphometric measurements of craters and basins on Mercury and the Moon from MESSENGER and LRO altimetry and image data: an observational framework for evaluating models of peak-ring basin formation. Planet. Space Sci. 86, 91–116. http://dx.doi.org/10.1016/j.pss.2013.07.003.

Britt, D.T., Yeomans, D.K., Housen, K.R., Consolmagno, G., 2002. Asteroid density, porosity and structure. In: Bottke, W., Cellino, A., Paolicchi, P., Binzel, R. (Eds.), Asteroids III. University of Arizona Press, Tucson, pp. 485–501.

Brož, P., Čadek, O., Hauber, E., Rossi, A.P., 2014. Shape of scoria cones on Mars: insights from numerical modeling of ballistic pathways. Earth Planet. Sci. Lett. 406, 14–23. http://dx.doi.org/10.1016/j.epsl.2014.09.002.

Brož, P., Hauber, E., 2012. A unique volcanic field in Tharsis, Mars: pyroclastic cones as evidence for explosive eruptions. Icarus 218 (1), 88–99. http://dx.doi.org/10.1016/j.icarus.2011.11.030.

Collins, G.S., Melosh, H.J., Ivanov, B.A., 2004. Modeling damage and deformation in impact simulations. Meteorit. Planet. Sci. 39 (2), 217–231. http://dx.doi.org/10.1111/j.1945-5100.2004.tb00337.x.

Denevi, B.W., Ernst, C.M., Meyer, H.M., Robinson, M.S., Murchie, S.L., Whitten, J.L., Head, J.W., Watters, T.R., Solomon, S.C., Ostrach, L.R., Chapman, C.R., Byrne, P.K., Klimczak, C., Peplowski, P.N., 2013. The distribution and origin of smooth plains

on Mercury. J. Geophys. Res. Planets 118 (5), 891–907. http://dx.doi.org/10.1002/jgre.20075.
Denevi, B.W., Robinson, M.S., Solomon, S.C., Murchie, S.L., Blewett, D.T., Domingue, D.L., McCoy, T.J., Ernst, C.M., Head, J.W., Watters, T.R., Chabot, N.L., 2009. The evolution of Mercury's crust: a global perspective from MESSENGER. Science (New York, N.Y.) 324 (5927), 613–618. http://dx.doi.org/10.1126/science.1172226.
Fraser, G.W., Carpenter, J.D., Rothery, D.a., Pearson, J.F., Martindale, A., Huovelin, J., Treis, J., Anand, M., Anttila, M., Ashcroft, M., Benkoff, J., Bland, P., Bowyer, A., Bradley, A., et al., 2010. The Mercury imaging X-ray spectrometer (MIXS) on BepiColombo. Planet. Space Sci. 58 (1-2), 79–95. http://dx.doi.org/10.1016/j.pss.2009.05.004.
Gaddis, L.R., Weller, L., Barrett, J., Kirk, R., Milazzo, M., Laura, J., Hawke, B.R., Giguere, T., Horgan, B., Bennett, K., 2013, "New" volcanic features in lunar, floor-fractured Oppenheimer crater. In: Lunar and Planetary Institute Science Conference, vol. 44, p. 2262.
Giacomini, L., Massironi, M., Marchi, S., Fassett, C.I., G, D.A., Cremonese, G., 2014. Dating a thrust system on Mercury: implications for the planet's thermal evolution. In: Platz, T., Massironi, M., Byrne, P.K., Hiesinger, H. (Eds.), Volcanism and Tectonism Across the Inner Solar System. Geological Society, London, p. 269 (Special Publications).
Gillis-Davis, J.J., Blewett, D.T., Gaskell, R.W., Denevi, B.W., Robinson, M.S., Strom, R.G., Solomon, S.C., Sprague, A.L., 2009. Pit-floor craters on Mercury: evidence of near-surface igneous activity. Earth Planet. Sci. Lett. 285 (3–4), 243–250. http://dx.doi.org/10.1016/j.epsl.2009.05.023.
Goudge, T.a., Head, J.W., Kerber, L., Blewett, D.T., Denevi, B.W., Murchie, S.L., Izenberg, N.R., Mcclintock, E., Holsclaw, G.M., Domingue, D.L., Gillis-Davis, J.J., Xiao, Z., Strom, R.G., Solomon, S.C., et al., 2014. Global inventory and characterization of pyroclastic deposits on Mercury: new insights into pyroclastic activity from MESSENGER orbital data. J. Geophys. Res. Planets 1325, http://dx.doi.org/10.1002/2013JE004480.
Hasenaka, T., Carmichael, I.S.E., 1985. The cinder cones of Michoacan–Guanajuato: central Mexico: their age, volume and distribution, and magma discharge rate. J. Volcanol. Geotherm. Res. 25, 105–124.
Head, J.W., Murchie, S.L., Prockter, L.M., Robinson, M.S., Solomon, S.C., Strom, R.G., Chapman, C.R., Watters, T.R., McClintock, W.E., Blewett, D.T., Gillis-Davis, J.J., 2008. Volcanism on Mercury: evidence from the first MESSENGER flyby. Science 321, 69–72. http://dx.doi.org/10.1016/j.icarus.2008.04.018.
Head, J.W., Wilson, L., 1979, Alphonsus-type dark-halo craters: morphology, morphometry and eruption conditions.In: Lunar and Planetary Science Conference Proceedings, vol. 10, pp. 2861–2897.
Head, J.W.I., Wilson, L., Pieters, C.M., 2000, Pyroclastic eruptions associated with the floor-fractured lunar farside crater Oppenheimer in the South Pole Aitken Basin. In: Lunar and Planetary Science XXXI, no. 1280.
Ivanov, B.A., Kostuchenko, V.N., 1997, Block oscillation model for impact crater collapse.In: Lunar and Planetary Science XXVIII, vol. 1655.
Jenness, J., 2011. Tools for Graphics and Shapes: Extension for ArcGIS. Jenness Enterprises.
Jozwiak, L.M., Head, J.W., Zuber, M.T., Smith, D.E., Neumann, G.a., 2012. Lunar floor-fractured craters: classification, distribution, origin and implications for magmatism and shallow crustal structure. J. Geophys. Res. 117 (E11), E11005. http://dx.doi.org/10.1029/2012JE004134.
Kenkmann, T., Poelchau, M.H., Wulf, G., 2014. Structural geology of impact craters. J. Struct. Geol. 62, 156–182. http://dx.doi.org/10.1016/j.jsg.2014.01.015.
Kerber, L., Head, J.W., Blewett, D.T., Solomon, S.C., Wilson, L., Murchie, S.L., Robinson, M.S., Denevi, B.W., Domingue, D.L., 2011. The global distribution of pyroclastic deposits on Mercury: the view from MESSENGER flybys 1–3. Planet. Space Sci. 59 (15), 1895–1909. http://dx.doi.org/10.1016/j.pss.2011.03.020.
Kerber, L., Head, J.W., Solomon, S.C., Murchie, S.L., Blewett, D.T., Wilson, L., 2009. Explosive volcanic eruptions on Mercury: eruption conditions, magma volatile content, and implications for interior volatile abundances. Earth Planet. Sci. Lett. 285 (3-4), 263–271. http://dx.doi.org/10.1016/j.epsl.2009.04.037.
Marchi, S., Massironi, M., Cremonese, G., Martellato, E., Giacomini, L., Prockter, L., 2011. The effects of the target material properties and layering on the crater chronology: the case of Raditladi and Rachmaninoff basins on Mercury. Planet. Space Sci. 59 (15), 1968–1980. http://dx.doi.org/10.1016/j.pss.2011.06.007.
Marchi, S., Morbidelli, A., Cremonese, G., 2005. Flux of meteoroid impacts on Mercury. Astron. Astrophys. 431, 1123–1127. http://dx.doi.org/10.1051/0004-6361:20041800.
McGetchin, T.R., Settle, M., Chouet, B.a., 1974. Cinder cone growth modeled after Northeast Crater, Mount Etna, Sicily. J. Geophys. Res. 79 (23), 3257–3272. http://dx.doi.org/10.1029/JB079i023p03257.
Melosh, H.J., Ryan, E.V., Asphaug, E., 1992. Dynamic fragmentation in impacts: hydrocode simulation of laboratory impacts. J. Geophys. Res. 97, 14735–14759.
Metrich, N., Wallace, P.J., 2008. Volatile abundances in basaltic magmas and their degassing paths tracked by melt inclusions. Rev. Mineral. Geochem. 69 (1), 363–402. http://dx.doi.org/10.2138/rmg.2008.69.10.
Moratto, S.Z.M., Broxton, M.J., Beyer, R.A., Lundy, M., Husmann, K., 2010. Ames Stereo Pipeline, NASA's open source automated stereogrammetry. Lunar and Planetary Science Conference vol. 41, 2364.
Nittler, L.R., Starr, R.D., Weider, S.Z., McCoy, T.J., Boynton, W.V., Ebel, D.S., Ernst, C. M., Evans, L.G., Goldsten, J.O., Hamara, D.K., Lawrence, D.J., McNutt, R.L., Schlemm, C.E., Solomon, S.C., et al., 2011. The major-element composition of Mercury's surface from MESSENGER X-ray spectrometry. Science (New York, N.Y.) 333 (6051), 1847–1850. http://dx.doi.org/10.1126/science.1211567.
Parfitt, E.a., Wilson, L., Head, J.W., 1993. Basaltic magma reservoirs: factors controlling their rupture characteristics and evolution. J. Volcanol. Geotherm. Res. 55 (1-2), 1–14. http://dx.doi.org/10.1016/0377-0273(93)90086-7.
Pierazzo, E., Artemieva, N., Asphaug, E., Baldwin, E.C., Cazamias, J., Coker, R., Collins, G.S., Crawford, D.a., Davison, T., Elbeshausen, D., Holsapple, K.a., Housen, K.R., Korycansky, D.G., Wünnemann, K., 2008. Validation of numerical codes for impact and explosion cratering: impacts on strengthless and metal targets. Meteorit. Planet. Sci. 43 (12), 1917–1938. http://dx.doi.org/10.1111/j.1945-5100.2008.tb00653.x.
Pierazzo, E., Collins, G., 2004. A brief introduction to hydrocode modeling of impact cratering. In: Dypvik, H., Burchell, M.J., Claeys, P. (Eds.), Cratering in Marine Environments and on Ice. Springer, Berlin Heidelberg, pp. 323–340.
Pike, R.J., 1988. Geomorphology of Impact Craters on Mercury. In: Vilas, F., Chapman, C.R., Matthews, M.S. (Eds.), Mercury. University of Arizona Press, Tucson, AZ, pp. 165–273.
Re, C., Roncella, R., Forlani, G., Cremonese, G., Naletto, G., 2012. Evaluation of area-based image matching applied to DTM generation with HIRISE images. Int. Arch. Photogramm. Remote Sens. Spatial Inf. Sci. 39, 209–214.
Rothery, D., Marinangeli, L., Anand, M., Carpenter, J., Christensen, U., Crawford, I.a., Sanctis, M.C. De, Epifani, E.M., Erard, S., Frigeri, A., Fraser, G., Hauber, E., Helbert, J., Hiesinger, H., et al., 2010. Mercury's surface and composition to be studied by BepiColombo. Planet. Space Sci. 58 (1-2), 21–39. http://dx.doi.org/10.1016/j.pss.2008.09.001.
Rothery, D.A., Thomas, R.J., Kerber, L., 2014. Prolonged eruptive history of a compound volcano on Mercury: volcanic and tectonic implications. Earth Planet. Sci. Lett. 385, 59–67.
Scholz, C.A., Karp, T., Brooks, K.M., Milkereit, Bernd, Amoako, P.Y.O., Arko, J.A., 2002. Pronounced central uplift identified in the Bosumtwi impact structure, Ghana, using multichannel seismic reflection data. Geology 30 (10), 939–942.
Schultz, R.A., 1993. Brittle strength of basaltic rock masses with applications to Venus. J. Geophys. Res. 98 (E6), 10883–10895. http://dx.doi.org/10.1029/93JE00691.
Schultz, P.H., 1976. Floor-fractured lunar craters. Moon 15, 241–273. http://dx.doi.org/10.1007/BF00562240.
Senft, L.E., Stewart, S.T., 2009. Dynamic fault weakening and the formation of large impact craters. Earth Planet. Sci. Lett. 287 (3-4), 471–482. http://dx.doi.org/10.1016/j.epsl.2009.08.033.
Spudis, P.D., Guest, J.E., 1988. Stratigraphy and Geologic History of Mercury. In: Vilas, F., Chapman, C.R., Matthews, M.S. (Eds.), Mercury. Unversity of Arizona Press, Tucson, AZ, p. 118.164.
Strom, R.G., Trask, N.J., Guest, J.E., 1975. Tectonism and volcanism on Mercury. J. Geophys. Res. 80 (17), 2478–2507. http://dx.doi.org/10.1029/JB080i017p02478.
Thomas, R.J., Rothery, D.A., Conway, S.J., Anand, M., 2014. Mechanisms of explosive volcanism on Mercury: implications from its global distribution and morphology. J. Geophys. Res. Planets.
Thompson, S.L., Lauson, H.S., 1974, Improvements in the Chart-D Radiationhydrodynamic Code III: Revised Analytic Equations of State: Sandia Labs. No. SC-RR–71-0714.
Weider, S.Z., Nittler, L.R., Starr, R.D., McCoy, T.J., Stockstill-Cahill, K.R., Byrne, P.K., Denevi, B.W., Head, J.W., Solomon, S.C., 2012. Chemical heterogeneity on Mercury's surface revealed by the MESSENGER X-ray spectrometer. J. Geophys. Res. 117, 1–15. http://dx.doi.org/10.1029/2012JE004153.
Wilson, L., Head, J.W., 1981. Ascent and eruption of basaltic magma on the Earth and Moon. J. Geophys. Res. 86 (B4), 2971–3001.
Wilson, L., Head, J.W., Tye, A.R., 2014. Lunar regional pyroclastic deposits: evidence for eruption from dikes emplaced into the near-surface crust. Lunar and Planetary Science Conference vol. 45, 1223.
Wilson, L., Sparks, R.S.J., Walker, G.P.L., 1980. Explosive volcanic eruptions—IV. The control of magma properties and conduit geometry on eruption column behaviour. Geophys. J. R. Astron. Soc., 117–148.
Wünnemann, K., Collins, G.S., Melosh, H.J., 2006. A strain-based porosity model for use in hydrocode simulations of impacts and implications for transient crater growth in porous targets. Icarus 180 (2), 514–527. http://dx.doi.org/10.1016/j.icarus.2005.10.013.
Wünnemann, K., Ivanov, B.a., 2003. Numerical modelling of the impact crater depth-diameter dependence in an acoustically fluidized target. Planet. Space Sci. 51 (13), 831–845. http://dx.doi.org/10.1016/j.pss.2003.08.001.
Zolotov, M.Y., 2011. On the chemistry of mantle and magmatic volatiles on Mercury. Icarus 212 (1), 24–41. http://dx.doi.org/10.1016/j.icarus.2010.12.014.